Chemical Science

ROYAL SOCIETY OF CHEMISTRY

EDGE ARTICLE

View Article Online
View Journal

Cite this: DOI: 10.1039/d6sc03172b

All publication charges for this article have been paid for by the Royal Society of Chemistry

Electrophilic N, P co-doped carbon enabling highly reversible iodine redox chemistry for ultra-stable bismuth-based zinc-ion batteries

Dandan Ling,[a] Yan Ma,[a] Liu Jiang,[a] Tong Zhou,*[bd] Daohong Zhang *[ac] and Qiufan Wang *[ac]

The pursuit of high-performance cathode materials is paramount for the deployment of aqueous zinc-ion batteries (ZIBs) in large-scale energy storage. Despite their high theoretical capacity and cost-effectiveness, bismuth (Bi)-based electrodes are often hampered by inferior cycling stability and sluggish redox kinetics. Herein, we report a composite cathode structure consisting of bismuth nanoparticles encapsulated within an N, P co-doped carbon framework (Bi@NPC), complemented by an iodide-based redox electrolyte additive to synergistically boost electrochemical performance. The integration of I^- ions activates a highly reversible I^0/I^- redox couple, which provides additional capacity and accelerates charge transfer. Density functional theory (DFT) calculations elucidate that the N, P co-doped carbon matrix offers enriched electrophilic active sites, which not only catalyze the transformation of iodine species but also effectively mitigate the "shuttle effect" of polyiodide intermediates. Consequently, the Bi@NPC electrode delivers a superior specific capacity of 399.3 mAh g^{-1} at 1.0 A g^{-1} and demonstrates exceptional long-term durability, maintaining 95.4% capacity retention after 10 000 cycles at 5.0 A g^{-1}. As a proof of concept, a flexible 3D interdigital Zn//Bi@NPC battery was assembled to power a Bi@NPC-based photodetector, highlighting its practical viability. This study provides a robust strategy for engineering high-capacity and ultra-stable bismuth-based energy storage systems.

Received 16th April 2026
Accepted 26th May 2026

DOI: 10.1039/d6sc03172b

rsc.li/chemical-science

Introduction

Energy storage systems (ESS) are pivotal in advancing the sustainable evolution of modern society.[1–3] Owing to their intrinsic safety, cost-effectiveness, and environmental benignity, aqueous ion batteries have emerged as formidable candidates for large-scale energy storage.[4,5] Specifically, aqueous zinc-ion batteries (ZIBs) offer distinct advantages, including an optimal redox potential and high theoretical capacity.[6,7] However, the practical deployment of ZIBs is frequently impeded by suboptimal electrode stability and limited cycling endurance. Conventional cathode systems, such as manganese-based compounds, vanadium oxides, and Prussian blue analogues, typically suffer from sloping discharge plateaus and active material dissolution, which undermine the long-term electrochemical stability.[8] This has necessitated the exploration of alternative cathode architectures that harmonize high specific capacity with robust structural integrity.

Bismuth (Bi), with a layered structure, has attracted interest in energy storage applications, including lithium-ion batteries, sodium-ion batteries, nickel/bismuth batteries and other energy storage fields.[9–11] These properties suggest that Bi may also offer promising performance for zinc-ion storage. For instance, Wang *et al.* designed a MXene/Bi cathode for aqueous ZIBs that delivered a specific discharge capacity of 178.1 mAh g^{-1} at 0.25 A g^{-1}.[12] Nevertheless, the application of Bi in near-neutral aqueous electrolytes remains constrained by sluggish charge-transfer kinetics and a relatively low discharge plateau (<0.8 V) compared to Mn-based or V-based oxides, which limits the overall energy density. Carbon hybridization has been identified as a viable approach to suppress Bi dissolution *via* physical confinement.[13] Furthermore, the introduction of iodine—an abundant, low-toxicity element—offers a promising pathway to augment capacity through the reversible I^0/I^- redox couple.[14] Fan *et al.* introduced iodide ions as a multifunctional electrolyte additive, enabling the reversible multi-electron conversion reaction between Bi(0) and Bi(III) in a mild aqueous electrolyte.[15] The iodide ions significantly alter the intermediate reaction steps and create a favorable kinetic pathway by coordinating

[a]Key Laboratory of Catalysis and Energy Materials, Chemistry of Ministry of Education, Hubei Key Laboratory of Catalysis and Materials Science, Hubei R&D Center of Hyperbranched Polymers Synthesis and Applications, South-Central Minzu University, Wuhan 430074, China. E-mail: daohong.zhang@scuec.edu.cn; ygdf@mail.scuec.edu.cn

[b]Hubei Key Laboratory of Energy Storage and Power Battery, School of New Energy, Hubei University of Automotive Technology, Shiyan 442002, China. E-mail: zhoutong1018@huat.edu.cn

[c]Guangdong Provincial Laboratory of Chemistry and Fine Chemical Engineering Jieyang Center, Jieyang 515200, China

[d]Key Laboratory of Advanced Energy Materials Chemistry, Nankai University, Tianjin 300071, China

with Bi^{3+} ions, which continuously refreshes and activates the interface. Therefore, introducing an iodine-based redox mediator into aqueous ZIBs presents a feasible strategy to enhance the electrochemical performance of Bi-based materials.

Herein, we propose a synergistic strategy employing low-concentration I^- additives to activate bismuth nanoparticles encapsulated within an N, P co-doped carbon framework (Bi@NPC) for high-performance ZIBs. The N, P co-doped carbon layer acts as a buffer layer to mitigate mechanical strain of Bi nanoparticles during Zn^{2+} insertion/extraction and enhances active material utilization. Critically, density functional theory (DFT) calculations reveal that N, P co-doping induces enriched electrophilic sites on the carbon skeleton. These sites intensify electron localization, thereby strengthening the adsorption of iodine species and catalyzing their multi-step conversion—effectively mitigating the polyiodide shuttle effect. The Bi@NPC electrode achieved a specific discharge capacity of 399.3 mAh g^{-1} at 1.0 A g^{-1}, and retained 95.4% of its capacity after 10, 000 cycles at 5.0 A g^{-1}. This provides a promising strategy for designing high-performance bismuth-based materials for advanced aqueous ZIBs.

Results and discussion

The introduction of a low-concentration (0.2 M) KI electrolyte additive effectively activates the conversion reactions of the Bi@NPC electrode. In the low-voltage region (0.1–1.2 V), the mechanism is dominated by the successive Zn^{2+}/H^+ intercalation/de-intercalation processes within the Bi matrix, accompanied by the reversible Bi/BiOI conversion reaction. In the high-voltage region (1.2–1.6 V), the electrochemical behavior is dominated by the conversion reactions of iodine species occurring on the NPC surface framework (Fig. 1a). To elucidate this enhanced electrochemical activity, cyclic voltammetry (CV) measurements were performed on the Bi@NPC electrode at a scan rate of 1 mV s^{-1} in two distinct electrolytes: 2 M $ZnSO_4$ and 2 M $ZnSO_4$ + 0.2 M KI (Fig. 1b and c). In the baseline 2 M $ZnSO_4$ electrolyte, the CV curve exhibits two pairs of redox peaks at 0.53/0.95 V and 0.68/0.87 V, which are assigned to Zn^{2+} and H^+ insertion/extraction processes, respectively (Fig. 1b). In contrast, upon addition of KI, a significant increase in the cathodic and anodic current response is observed within the 0.1–1.2 V range, along with the emergence of additional redox peaks between 1.2–1.6 V range (Fig. 1c). These new observed electrochemical features are attributed to the activation of the Bi/BiOI redox couple and the multi-step conversion reactions of iodine species. The introduction of this redox-active electrolyte additive not only extends the operating voltage window but also contributes additional capacity through faradaic reactions. More importantly, it mitigates the polyiodide shuttle effect and facilitates the stepwise conversion of iodine intermediates (Fig. 1d). Schematic representations of

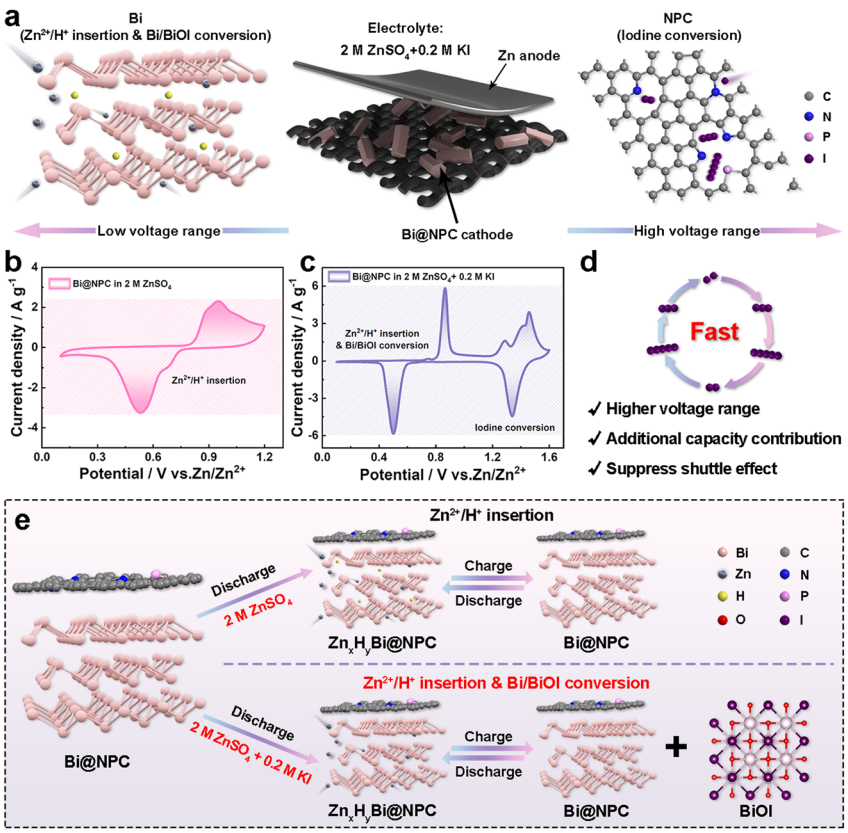

Fig. 1 (a) Schematic diagram of the energy storage mechanism of the Zn//Bi@NPC battery at different potentials. (b and c) CV curves of the Zn//Bi@NPC battery in different electrolytes at 1.0 mV s^{-1}. (d) Proposed transformation pathway of iodine species. (e) Illustration of the charge storage mechanism in the Bi@NPC electrode with and without KI additive.

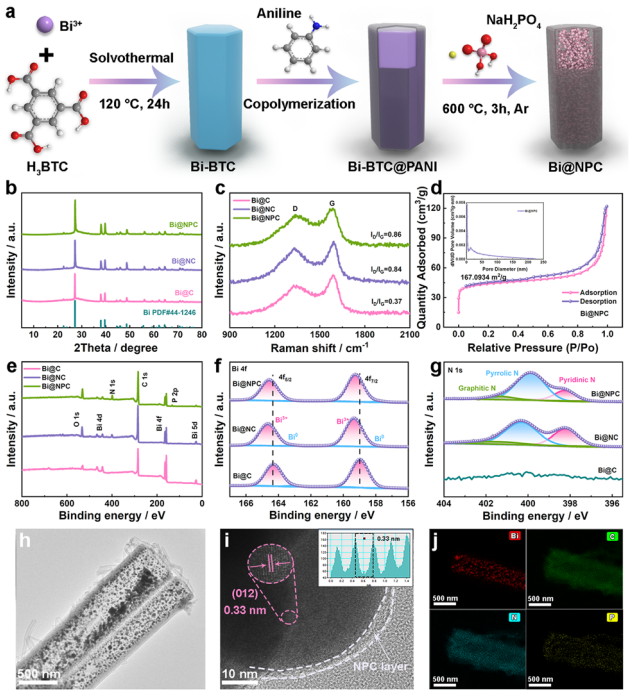

Fig. 2 (a) Schematic illustration of the synthesis of Bi@NPC. (b) XRD patterns, and (c) Raman spectra of Bi@C, Bi@NC and Bi@NPC. (d) N_2 adsorption–desorption isotherms of Bi@NPC. (e) XPS survey spectra, (f) Bi 4f and (g) N 1s XPS spectra of Bi@C, Bi@NC and Bi@NPC. (h) TEM image, (i) HRTEM images and (j) element mapping of Bi@NPC.

the charge storage mechanisms in the two electrolyte systems are summarized in Fig. 1e. While the mechanism in the pure $ZnSO_4$ electrolyte is limited to Zn^{2+}/H^+ insertion/extraction (Fig. S1), the presence of KI enables additional reversible conversion reactions involving both Bi/BiOI and iodine species, which will be further elaborated in subsequent sections.

Fig. 2a presents the synthesis process of Bi@NPC. Bi-1,3,5-benzenetricarboxylic acid (Bi-BTC)-derived N, P co-doped carbon nanorods embedded with Bi nanoparticles were synthesized *via* a facile solvothermal method. The composite exhibits a highly conductive surface architecture and rich active sites. In addition, the N, P co-doped carbon layer effectively accommodates mechanical strain during repeated cycling, thereby significantly enhancing the cycling stability.[16] The crystal structure of the materials was examined using X-ray diffraction (XRD) (Fig. 2b). Bi@C, Bi@NC and Bi@NPC all show distinct diffraction peaks that match well with the hexagonal phase of metallic Bi (PDF#44-1246). Fourier-transform infrared (FTIR) spectra were used to analyze the chemical structures of Bi-BTC and Bi-BTC@PANI (Fig. S2). In Bi-BTC@PANI, the peak at 1490 cm^{-1} corresponds to the C=C stretching vibration of the benzene ring, and the peak at 1145 cm^{-1} is assigned to the C–H bending vibration of the benzene and quinoid rings.[17] Further structural information was investigated using Raman spectroscopy (Fig. 2c). The higher I_D/I_G ratio of Bi@NPC indicates the introduction of abundant defects in its carbon network.[18] N_2 adsorption–desorption isotherms (Fig. 2d and S3) show that Bi@NPC nanorods have a larger specific surface area, which is beneficial for the rapid transport of Zn^{2+}. Subsequently, X-ray photoelectron spectroscopy (XPS) was utilized to analyse the surface composition of the samples (Fig. 2e–g and S4). In the Bi 4f XPS spectrum (Fig. 2e), the two fitted peaks at 157.86 and 163.54 eV correspond to Bi^0, while the two peaks at 159.25 and 164.56 eV correspond to Bi^{3+}. The presence of Bi^{3+} is attributed to the inevitable surface oxidation of Bi during synthesis, which is consistent with previous reports.[19] Compared with Bi@C, the Bi 4f peaks in Bi@NC and Bi@NPC shift to higher binding energies. This shift is mainly due to the higher electronegativity of N, which reduces the electron cloud density around Bi atoms. As shown in Fig. 2f, the N 1s peaks detected in Bi@NPC at 397.75, 399.37, and 400.85 eV can be attributed to pyridinic N, pyrrolic N, and graphitic N, respectively.[20] In contrast, almost no N 1 s signal was detected in Bi@C. The relative percentages of these N species in Bi@NC and Bi@NPC are provided in Fig. S5. Additionally, the C 1s and O 1s spectra are presented in Fig. S4.

The morphology of the samples was characterized by scanning electron microscopy (SEM) and transmission electron microscopy (TEM) (Fig. 2h–j and S5–S8). As shown in Fig. S6, the precursor Bi-BTC exhibits a smooth and uniform nanorod structure. After high-temperature carbonization, the derived Bi@NPC still maintains the nanorod structure well, with ultrafine and homogeneously dispersed Bi nanoparticles with a diameter of approximately 30–50 nm encapsulated inside (Fig. 2h). Compared with Bi@C and Bi@NC, Bi@NPC exhibits a thicker carbon layer on the surface (Fig. S7–S9). The loose and porous nanorod structure can effectively mitigate structural fracture and pulverization during Zn^{2+} insertion/extraction, while also offering a high specific surface area to facilitate efficient ion transport. The high-resolution TEM (HRTEM) image in Fig. 2h reveals lattice fringes with a spacing of approximately 0.33 nm, corresponding to the (012) plane of metallic Bi. A carbon layer coating the Bi nanoparticles is highlighted by blue lines. Elemental mappings in Fig. 2i confirm the uniform distribution of Bi, N, P and C throughout the entire nanorod, indicating the successful co-doping of N and P.

To investigate the effects of KI as an electrolyte additive on the zinc storage performance and the role of N, P co-doped carbon in stabilizing bismuth nanoparticles, a series of electrochemical tests were carried out. Cyclic voltammetry (CV) and galvanostatic charge–discharge (GCD) measurements of Bi@C, Bi@NC and Bi@NPC electrodes were performed in a 2 M $ZnSO_4$ + 0.2 M KI electrolyte within a voltage window of 0.1–1.6 V (Fig. 3a, b, S10 and S11). The redox peaks observed at 0.50/0.87 V can be attributed to the redox reaction of Bi/Bi^{3+}, while the redox peaks at 1.34/1.46 V correspond to the I^0/I^- reaction (Fig. 3a). Notably, the additional oxidation peak appearing at 1.29 V may arise from iodine vacancies generated during the electrochemical process.[21] Compared with Bi@C and Bi@NC, Bi@NPC electrode exhibits a significantly larger integrated area under the I^0/I^- redox peaks in the CV profiles, indicating enhanced charge storage activity. This improvement is further corroborated by the GCD curves (Fig. 3b). To better evaluate the

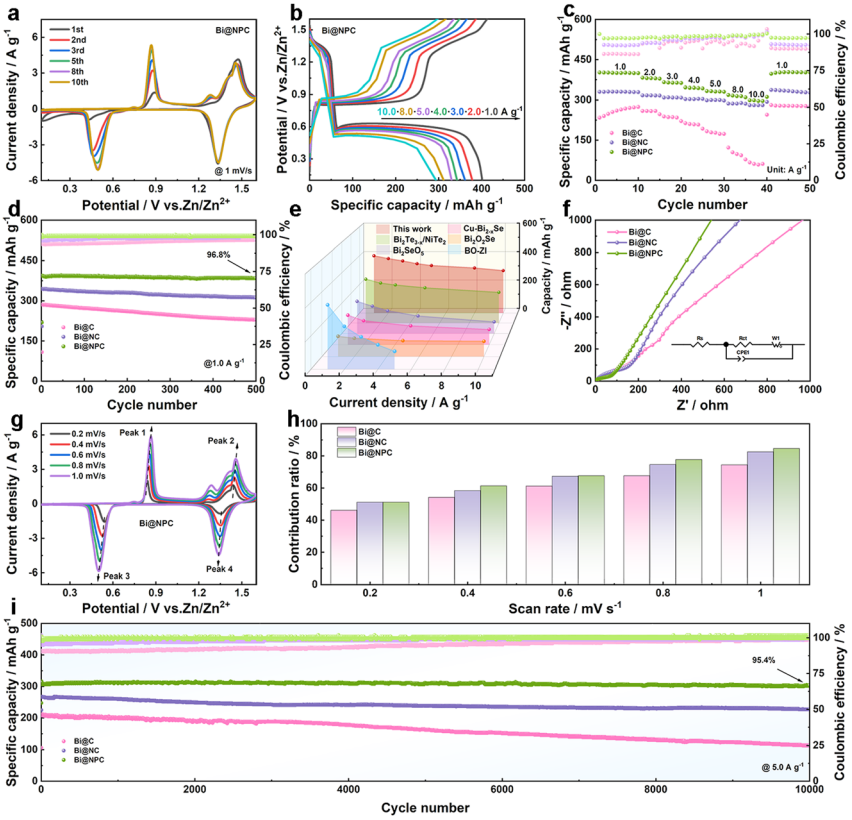

Fig. 3 (a) CV curve of Bi@NPC electrode at 1 mV s^{-1}. (b) GCD curves of Bi@NPC electrode at various current densities. (c) Rate performance and (d) cycle performance at 1.0 A g^{-1} of the Bi@C, Bi@NC and Bi@NPC electrodes, respectively. (e) Comparison of electrochemical performance between Bi@NPC electrode and other reported bismuth-based electrodes. (f) EIS spectra of Bi@C, Bi@NC and Bi@NPC electrodes. (g) CV curves of Bi@NPC electrode at scan rates from 0.2 to 1.0 mV s^{-1}. (h) Comparison of the capacitive contributions of Bi@C, Bi@NC and Bi@NPC electrodes. (i) Long-term cycling performance of Bi@C, Bi@NC and Bi@NPC electrodes at 5.0 A g^{-1}.

electrochemical advantages of the redox additive KI and the NPC layer, rate and cycling tests were conducted. As shown in Fig. 3c and S12, Bi@NPC electrode delivers a specific capacity of 399.3 mAh g^{-1} at 1.0 A g^{-1}, which exceeds that of Bi@C (274.2 mAh g^{-1}) and that of Bi@NC electrode (329.5 mAh g^{-1}). Even at a high current density of 10.0 A g^{-1}, Bi@NPC electrode maintains a discharge capacity of 296.1 mAh g^{-1}, showing superior rate capability. In contrast, the Bi@C electrode exhibits significant capacity degradation at higher current densities. In addition, to evaluate the individual contribution of the carbon components, its electrochemical performance was tested in the same electrolyte (Fig. S11). The observed capacity is mainly attributed to the reversible redox reaction of iodine species on the surface of NPC electrodes. After 500 cycles at 1.0 A g^{-1} (Fig. 3d), Bi@NPC electrode retains a near 100% coulombic efficiency (CE) and a specific capacity of 384.1 mAh g^{-1}, corresponding to a 96.8% capacity retention. This performance significantly outperforms that of the Bi@C (84.9% retention, CE $\approx$ 94%) and Bi@NC (90.5% retention, CE $\approx$ 97%) electrodes. Compared with other bismuth-based ZIBs electrodes (Fig. 3e), the Bi@NPC electrode exhibits superior comprehensive performance.[22–26]

To further elucidate the effects of N, P-doped carbon layers and redox additives on electrochemical performance, reaction kinetics tests were performed on the electrodes in ZIBs. Electrochemical impedance spectroscopy (EIS) revealed that Bi@NPC possesses a lower charge transfer resistance and a higher ionic diffusion coefficient (Fig. 3f), underscoring the beneficial role of the NPC layer in enhancing ion transport and electrical conductivity. The CV curves of the Bi@C, Bi@NC and Bi@NPC electrodes at different scan rates (0.2–1.0 mV s^{-1}) are shown in Fig. 3g, S13 and S14. As depicted in Fig. 3g, the CV curves of the Bi@NPC electrode show minimal peak shifts and retain well-defined redox profiles even at high scan rates, suggesting low polarization and favorable reaction kinetics. The calculated *b* values for the Bi@NPC electrode are 0.66, 0.55, 0.83 and 1.03 (Fig. S15), indicating that the redox behaviors of Bi and I are controlled by diffusion and capacitive behavior. As shown in Fig. 3h, the capacitive contribution ratios of the Bi@NPC electrode reach 51.1%, 61.3%, 67.6%, 77.7%, and 84.6% at scan rates of 0.2, 0.4, 0.6, 0.8, and 1.0 mV s^{-1}, respectively. These values are higher than those of Bi@C (46.1%, 54.2%, 61.2%, 67.6%, and 74.4%) and Bi@NC (51.1%, 58.3%, 67.3%, 74.6%, and 82.5%). The increased capacitive contribution in Bi@NPC underscores the role of the NPC layer in promoting surface-controlled charge storage, facilitating faster charge transfer and improving rate capability. Moreover, after 10 000 cycles, Bi@NPC still achieves an outstanding 95.4% capacity retention

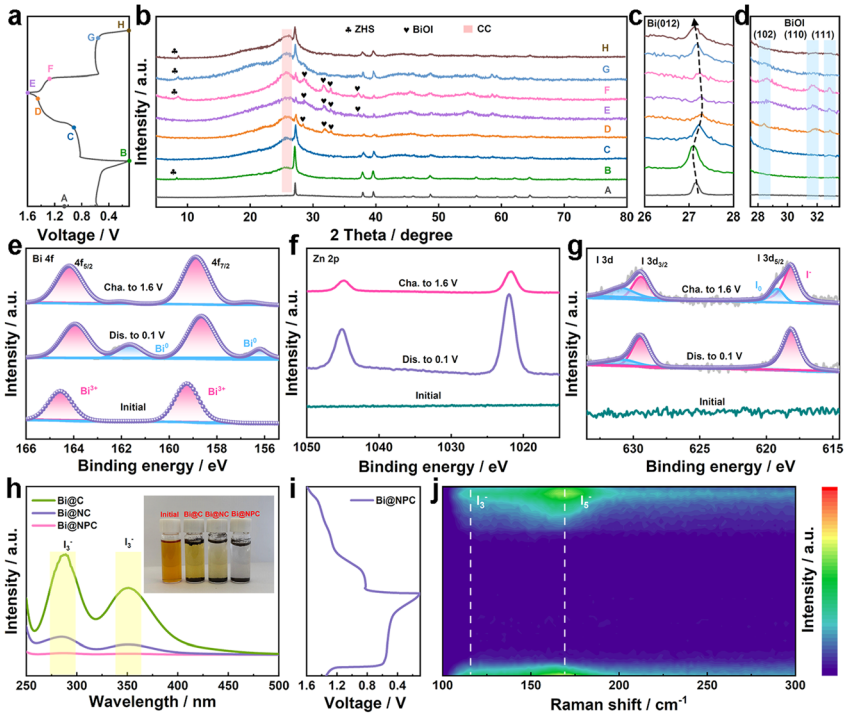

Fig. 4 Storage mechanism of Bi@NC electrode in $ZnSO_4$-KI electrolyte. (a) GCD curve and (b–d) corresponding *ex situ* XRD pattern. (e) Bi 4f, (f) Zn 2p and (g) I 3d XPS spectra in initial and charge–discharge states. (h) UV-Vis spectra and digital photos (illustrations) of Bi@C, Bi@NC and Bi@NPC after standing for 24 h in 2 M $ZnSO_4$ + 0.2 M KI electrolyte. (i) GCD curve and (j) corresponding *in situ* Raman spectra of Bi@NPC.

(Fig. 3i), highlighting its exceptional cycling stability. In contrast, the Bi@C electrode exhibited a significantly lower capacity retention of only 53.4%, which is primarily attributed to the substantial volume changes of the Bi nanoparticles during charging and discharging, leading to structural degradation and poor cycling stability.[27,28] In addition, the SEM images of Bi@C and Bi@NPC electrodes after cycling are shown in Fig. S16. In the Bi@NPC electrode, the NPC layer serves as a robust conductive network that effectively anchors the Bi nanoparticles, facilitates their reaction with iodide ions, and buffers the structural collapse caused by volume expansion. This multifunctional role collectively contributes to the superior electrochemical performance.

To evaluate the energy storage mechanism of the Bi@NPC electrode, *ex situ* XRD and XPS analyses were conducted. The first GCD curve of the Bi@NPC electrode is shown in Fig. 4a. During the initial discharge process (A and B), the diffraction peak at 27.16° shifts to a lower Bragg angle (Fig. 4b and c), indicating an expanded interlayer spacing resulting from Zn^{2+} insertion. Notably, a new diffraction peak emerges at 8.31°, corresponding to $ZnSO_4[Zn(OH)_2]_3 \cdot xH_2O$ (ZHS, PDF#78-0246), which implies concurrent H^+ insertion.[29] The subsequent charging process (B–E) demonstrates a reverse shift of the XRD peaks toward higher Bragg angles, confirming the extraction of Zn^{2+}. The disappearance of ZHS-related peaks indicates reversible H^+ extraction. Furthermore, new diffraction peaks appear at 28.67, 31.70, 32.81 and 37.23°, indexed to BiOI (PDF#10-0445), providing evidence of a conversion reaction (Fig. 4d). Additional support for this conversion is observed through the gradual decrease in intensity of metallic Bi peaks at 27.16, 37.94 and 39.61° during charging. In the following discharge process (E–H), the diffraction peak at 27.16° shifts back reversibly to lower angles with increasing intensity, while BiOI-related peaks diminish, confirming the reversible nature of the conversion reaction. XPS was used to characterize the valence states of Bi, Zn and I (Fig. 4e–g). After Zn^{2+} insertion, the intensity of Bi^0 peaks (156.20 and 161.64 eV) increases, while Bi $4f_{7/2}$ and Bi $4f_{5/2}$ peaks shift to lower binding energy (Fig. 4e). Upon Zn^{2+} extraction, the intensity of the peaks at 158.86 and 164.17 eV, attributed to Bi^{3+} increase, indicating the occurrence of the conversion reaction. In Zn 2p, the peaks at 1021.98 and 1045.13 eV in the discharge state correspond to Zn $2p_{3/2}$ and Zn $2p_{1/2}$, respectively (Fig. 4f), confirming successful Zn^{2+} intercalation. The decreased peak intensity in fully charged state is likely due to the residual adsorption of zinc ions from the electrolyte on the electrode surface.[30] Fig. 4g shows the I 3d spectrum, in which two pairs of peaks, 618.4/629.88 eV and 619.53/631.45 eV, can be assigned to I^- and I^0, respectively. Notably, the peak intensity of the I^0 peak increases when charging to 1.6 V and then decreases upon discharge to 0.9 V, indicating a reversible I^0/I^- redox reaction in Bi@NPC electrode. In order to further analyze the adsorption capacity of Bi@NPC for iodine species, a separate experiment was conducted. 10 mg of Bi@C, Bi@NC and Bi@NPC powders were added into 10 mL 2 M $ZnSO_4$ + 0.2 M KI electrolyte and allowed to stand for 24 h (inset of Fig. 4h). After 24 h, the supernatant of the control electrolyte turned brown, indicating polyiodide

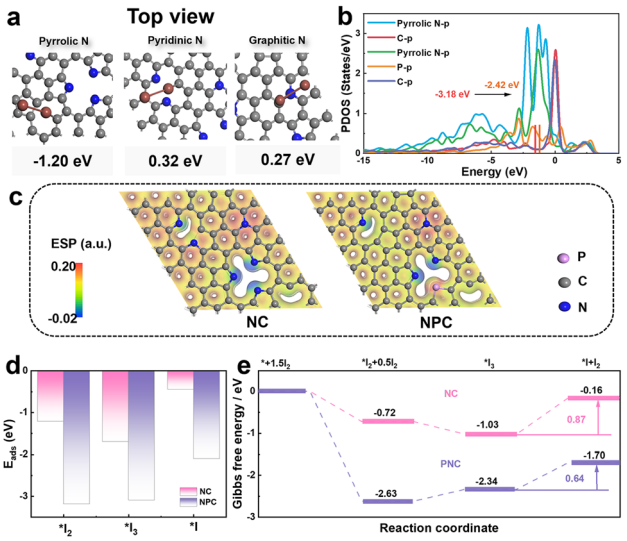

Fig. 5 (a) Adsorption configurations of I_2 on pyridinic N, pyrrolic N, and graphitic N sites. (b) Projected density of states (PDOS) plots for NC and NPC. (c) Electrostatic potential maps of NC and NPC. (d) Adsorption energies of NC and NPC for various iodine species. (e) Gibbs free energy diagrams for the iodine reduction reaction on NC and NPC.

formation. In contrast, the electrolyte with Bi@C became light yellow, and that with Bi@NPC became nearly colorless.

UV-vis spectra of the supernatants corroborate these observations, showing that Bi@NPC exhibits the highest adsorption capacity for I_3^- species, followed by Bi@NC and then Bi@C (Fig. 4h). To gain deeper insight into the confinement effect on iodine species, *in situ* Raman spectra was performed on the electrodes (Fig. 4i, j and S16). For the Bi@NPC electrode, the Raman peak observed at 166 cm^{-1} corresponds to the stretching vibration of I_5^-. When charging to 1.6 V, only a weak I_5^- signal is detected for Bi@NPC. In contrast, the Bi@C electrode exhibits strong signals for both I_3^- and I_5^- at the same potential (Fig. S17). This marked difference is attributed to the strong adsorption capability of Bi@NPC towards iodine species, which effectively suppresses the formation of soluble polyiodides.

To gain deeper insight into the electrochemical performance of Bi@NPC, density functional theory (DFT) calculations were performed. Based on the experimental and preliminary theoretical results, structural models for NC and NPC were constructed (Fig. S18). Fig. S19 presents the optimized geometric configurations of NPC and their relative energies. Among the considered configurations, the structure in which P occupies a pyrrolic N site exhibits the lowest energy and was therefore selected for all subsequent computational analyses. Fig. 5a displays the adsorption configurations and energies of iodine species on NC. The presence of pyrrolic N induces carbon vacancies, thereby reducing steric hindrance. Concurrently, the electron-withdrawing nature of pyrrolic N generates an electron-deficient state on adjacent carbon atoms, promoting electron localization and enhancing the adsorption strength of iodine species. Consequently, the sites adjacent to pyrrolic N exhibit the most negative adsorption energy. The projected density of states (PDOS) was calculated to elucidate changes in the electronic structure (Fig. 5b). Due to the lower electronegativity of P compared to N, the P-doped site exhibits a more pronounced electron-deficient character at the active sites. The incorporation of P shifts the p-band center upward from −3.18 eV to −2.42 eV, thereby enhancing the binding affinity toward iodine

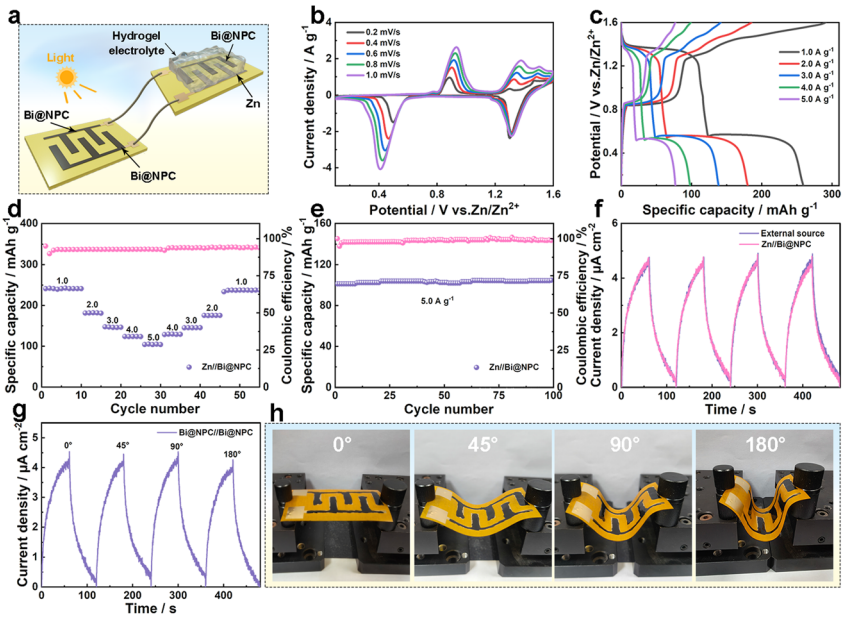

Fig. 6 (a) Schematic illustration of the self-integrated device comprising a 3D Bi@NPC interdigitated electrode and a photodetector. (b) CV curves, (c) GCD curves, (d) rate performance and (e) cycle performance at 5.0 A g^{-1} of the Zn//Bi@NPC interdigitated electrode. (f) Comparison of the photocurrent response between the self-powered integrated device and a photodetector driven by an external power source. (g) Photocurrent response of Bi@NPC//Bi@NPC flexible photodetector driven by Zn//Bi@NPC interdigital electrode at an applied voltage of 0.8 V under different bending conditions. (h) Photographs of the flexible photodetector under different bending angles.

species. Fig. 5c shows the electrostatic potential maps of NC and NPC. The introduction of P increases surface polarity, effectively modulating the electrostatic potential distribution. The region around P atoms shows a positive electrostatic potential, providing additional electrophilic sites that facilitate stronger adsorption and promotes conversion of iodine species. Furthermore, the interactions between various I_2-derived intermediates (*I_2, *I_3, and *I) and the carbon substrates are compared in Fig. 5d. NPC exhibits more negative adsorption energies for all species relative to NC, indicating enhanced binding with polyiodides. The Gibbs free energy profile for the iodine reduction reaction (to iodide ions) further confirms the superior catalytic activity of NPC over NC (Fig. 5e). For the rate-determining step (RDS, $I_3^- \rightarrow I^- + I_2$), the calculated Gibbs free energy barrier (ΔG) on NPC is 0.64 eV, lower than that on NC (0.87 eV). Thus, the incorporation of P effectively accelerates the kinetics of polyiodide conversion, thereby suppressing the shuttle effect of iodine species.

To demonstrate practical application, a flexible Zn//Bi@NPC 3D interdigital electrode was fabricated and integrated with a Bi@NPC-based photodetector to construct a self-powered system (Fig. 6a). The electrochemical performance of the interdigital electrode was evaluated. As shown in Fig. 6b, CV curves recorded at scan rates ranging from 0.2 to 1.0 mV s^{-1} retain a shape similar to that of the coin-cell configuration, with well-defined redox peaks preserved even at the highest scan rate. GCD profiles at various current densities display consistent charge/discharge plateaus (Fig. 6c), confirming that the interdigital device maintains the intrinsic electrochemical behavior of the Bi@NPC material and operates with high reversibility. The interdigital electrode delivers a specific capacity of 241.5 mAh g^{-1} at 1.0 A g^{-1} (Fig. 6d). When the current density is increased to 5.0 A g^{-1}, a capacity of 105.2 mAh g^{-1} is retained. Notably, upon returning the current density to 1.0 A g^{-1}, the capacity recovers to 237.5 mAh g^{-1}, demonstrating excellent rate capability and reversibility. The cycle stability of the device was evaluated at 5.0 A g^{-1} (Fig. 6e), showing excellent performance with a capacity retention of 99.22% after 100 cycles. Leveraging this robust electrochemical performance, the Zn//Bi@NPC interdigital electrode was successfully integrated with a flexible Bi@NPC//Bi@NPC photodetector to realize a self-powered device. Remarkably, the photocurrent response of the detector powered by this integrated electrode is comparable to that achieved under an external power source (Fig. 6f). Furthermore, the flexible self-powered device maintains stable photoresponse performance not only in the planar state but also under various bending conditions (Fig. 6g and h), highlighting its excellent mechanical durability and potential for wearable applications.

Conclusions

In conclusion, we have developed a novel conversion-type Bi@NPC cathode, which combined with halogen electrolyte additive strategy, showed high specific capacity and long-term cycling stability. The Bi nanoparticles are effectively anchored within a nitrogen and phosphorus co-doped carbon matrix, which alleviates mechanical strain during Zn^{2+} insertion/extraction cycles. DFT calculations confirm the strong adsorption capability of the N, P co-doped carbon for iodine species, elucidating a potential electrochemical energy storage mechanism. Specifically, the introduced iodide ions activate Bi–I bonding, leading to the formation of soluble Bi–I intermediates rather than direct solid-phase passivation products, thereby preventing the accumulation of electrochemically inactive Bi^{3+} species on the electrode. Additionally, the reversible I^0/I^- redox couple contributes extra capacity to the system. As expected, the Bi@NPC electrode delivers a remarkable specific capacity of 399.3 mAh g^{-1} at 1.0 A g^{-1} and maintains virtually no capacity decay over 10 000 cycles even at a high current density of 5.0 A g^{-1}. In addition, the assembled flexible Zn//Bi@NPC 3D interdigital electrode can be used as the power supply for the photodetector based on Bi@NPC, showing good photoelectric behavior and bending performance. This work provides fundamental new insights into the conversion reaction mechanism of bismuth-based materials in aqueous ion batteries.

Author contributions

Dandan Ling: data curation, investigation, methodology, writing – original draft. Yan Ma: data curation, investigation. Liu Jiang: investigation, methodology. Tong Zhou: software. Daohong Zhang: supervision, funding. Qiufan Wang: writing – review & editing.

Conflicts of interest

There are no conflicts to declare.

Data availability

The data that support the findings of this study are available on request from the corresponding author, upon reasonable request.

Supplementary information (SI): experimental details, SEM images, and electrochemical performance. See DOI: https://doi.org/10.1039/d6sc03172b.

Acknowledgements

The authors gratefully acknowledge the financial support from the National Natural Science Foundation of China (51702369, 22509055), Hubei Provincial Young Scientific and Technological Talent Cultivation Program (2025DJA042) and Fundamental Research Funds for the Central Universities of South-Central Minzu University (CZD24001).

Notes and references

1 X. Yang, H. Zhang, Q. Liu and G. Jiang, The Li-ion battery industry and its challenges, *Nat. Rev. Chem.*, 2025, **9**, 497–498.

2 Y. He, Y. Liu, W. Shang, Q. Ma, J. Wei and P. Tan, A decade-long odyssey of "rocking-chair" zinc-ion batteries, *Electrochem. Energy Rev.*, 2026, **9**, 1.
3 F. Degen, M. Winter, D. Bendig and J. Tübke, Energy consumption of current and future production of lithium-ion and post lithium-ion battery cells, *Nat. Energy*, 2023, **8**, 1284–1295.
4 Y. Liang and Y. Yao, Designing modern aqueous batteries, *Nat. Rev. Mater.*, 2022, **8**, 109–122.
5 Y. Zhao, Y. Wang, J. Li, J. Xiong, Q. Li, K. Abdalla, Y. Zhao, Z. Cai and X. Sun, Thermodynamic and kinetic insights for manipulating aqueous Zn battery chemistry: towards future grid-scale renewable energy storage systems, *eScience*, 2025, **5**, 100331.
6 M. Tang, Q. Liu, X. Zou, B. Zhang and L. An, High-energy-density aqueous zinc-ion batteries: Recent progress, design strategies, challenges, and perspectives, *Adv. Mater.*, 2025, **37**, 2501361.
7 L. Zhang, J. Xiao, X. Xiao, W. Xin, Y. Geng, Z. Yan and Z. Zhu, Molecular engineering of self-assembled monolayers for highly utilized Zn anodes, *eScience*, 2024, **4**, 100205.
8 A. Ali, J. Mohammadi Moradian, A. Naveed, S. Zhang, M. H. Tahir, K. Shehzad and M. Sillanpää, Progress in cathode materials for rechargeable zinc-ion batteries: from inorganic and organic systems to hybrid frameworks and biomass-derived innovations, *Prog. Mater. Sci.*, 2026, **156**, 101543.
9 X. Man, X. Min, Y. Yan, H. Gong, Y. Dai, T. Li, P. Xiao, Y. Sun, L. Yin and R. Wang, Prospect of bismuth and its compounds in sodium-ion batteries: A Review, *Energy Storage Mater.*, 2025, **75**, 104076.
10 D. Zhu, H. Zhu, H. Wu and C. Yang, Bismuth anode engineering for tomorrow's batteries: A review of cutting-edge strategies, *Energy Storage Mater.*, 2025, **75**, 103978.
11 H. Qian, Y. Liu, H. Chen, K. Feng, K. Jia, K. Pan, G. Wang, T. Huang, X. Pang and Q. Zhang, Emerging bismuth-based materials: From fundamentals to electrochemical energy storage applications, *Energy Storage Mater.*, 2023, **58**, 232–270.
12 Q. Wang, M. Wang, L. Wen, W. Zeng, B. Ge, C. Zhang, Y. Yue and S. Wang, A new (de)intercalation MXene/Bi cathode for ultrastable aqueous zinc-ion battery, *Adv. Funct. Mater.*, 2023, **34**, 2214506.
13 Y. Yu, H. Zhang, F. Yang, Y. Zeng, X. Liu and X. Lu, Bismuth nanoparticles@carbon composite as a stable and high capacity anode for high-voltage bismuth-manganese batteries, *Energy Storage Mater.*, 2021, **41**, 623–630.
14 X. Huang, Y. Dong, M. Zhou, L. Chen, T. Song, Y. Pei, X. Wang, B. Long, Q. Deng and X. Wu, Dual-mechanism aqueous battery with I^-/I_2 redox and Bi/BiOI conversion, *Adv. Energy Mater.*, 2025, **15**, e03253.
15 X. Luo, T. Xie, T. Fang, H. Liu, S. Zhang, M. Cen, W. Peng, Y. Li and X. Fan, Regulating the intermediate process of zinc–bismuth batteries by iodide ions, *ACS Energy Lett.*, 2023, **8**, 3569–3577.
16 J. Gao, G. Wang, W. Wang, L. Yu, B. Peng, A. El-Harairy, J. Li and G. Zhang, Engineering electronic transfer dynamics and ion adsorption capability in dual-doped carbon for high-energy potassium ion hybrid capacitors, *ACS Nano*, 2022, **16**, 6255–6265.
17 H. Dong, L. Wang, F. Zhang, H. Li, X. Zhao, W. Wei, Y. Kang, C. Yan, Y. Sang, H. Liu and S. Wang, Green proton reservoirs of PANI for disposable high-performance zinc-ion batteries, *Nano Energy*, 2024, **128**, 109768.
18 Y. Wang, X. Xu, Y. Wu, F. Li, W. Fan, Y. Wu, S. Ji, J. Zhao, J. Liu and Y. Huo, Facile galvanic replacement construction of Bi@C nanosheets array as binder-free anodes for superior sodium-ion batteries, *Adv. Energy Mater.*, 2024, **14**, 2401833.
19 R. Cui, H. Zhou, J. C. Li, C. Yang and Q. Jiang, Ball-cactus-like Bi embedded in N-riched carbon nanonetworks enables the best potassium storage performance, *Adv. Funct. Mater.*, 2021, **31**, 2103067.
20 Z. Yang, F. Lai, Q. Mao, C. Liu, R. Wang, Z. Lu, T. Zhang and X. Liu, Reversing zincophobic/hydrophilic nature of metal-N-C *via* metal-coordination interaction for dendrite-free Zn anode with high depth-of-discharge, *Adv. Mater.*, 2024, **36**, 2311637.
21 H. Xu, W. Gao, H. Dou, X. Zhang and M. Pumera, Photo-assisted Zn-iodine battery *via* bifunctional cathode with iodine host and solar response boost, *Adv. Funct. Mater.*, 2024, **35**, 2414022.
22 Y. Zong, H. Chen, J. Wang, M. Wu, Y. Chen, L. Wang, X. Huang, H. He, X. Ning, Z. Bai, W. Wen, D. Zhu, X. Ren, N. Wang and S. Dou, Cation defect-engineered boost fast kinetics of two-dimensional topological Bi_2Se_3 cathode for high-performance aqueous Zn-ion batteries, *Adv. Mater.*, 2023, **35**, 2306269.
23 Y. Chen, S. Wang, Y. Wang, Z. Fang, B. Liu, Y. Mi, J. Bai, B. Wang and G. Wang, Interfacial structuring of vacancy-rich $Bi_2Te_3/NiTe_2$ with substantial melioration on dual-ion storage property for aqueous zinc-based batteries, *J. Energy Chem.*, 2025, **105**, 130–141.
24 Y. Hsieh, Y. Chuang and H. Tuan, Unraveling dual mechanisms in quasi-layered Bi_2O_2Se *via* defect modulation for high-performance aqueous Zn-ion batteries, *Adv. Funct. Mater.*, 2024, **34**, 2406975.
25 Y. Cao, Y. Qian, L. Chen, T. Song, Y. Pei, X. Wang, X. Wu, Y. Dong, F. Liu and B. Long, Hollow Bi_2SeO_5 particles as high-performance insertion-type anodes for "rocking chair" zinc-ion batteries, *J. Energy Storage*, 2025, **125**, 116986.
26 N. Liu, Z. Liu, J. Li, Z. Ge, L. Fan, C. Zhao, Z. Guo, A. Chen, X. Lu, Y. Zhang, N. Zhang and X. Zhang, Unlocking the capacity of bismuth oxide by a redox mediator strategy for high-performance aqueous Zn-ion batteries, *ACS Appl. Mater. Interfaces*, 2023, **15**, 51170–51178.
27 L. Chen, X. He, H. Chen, S. Huang and M. Wei, N-Doped carbon encapsulating Bi nanoparticles derived from metal–organic frameworks for high-performance sodium-ion batteries, *J. Mater. Chem. A*, 2021, **9**, 22048–22055.
28 S. Wei, W. Li, Z. Ma, X. Deng, Y. Li and X. Wang, Novel bismuth nanoflowers encapsulated in N-doped carbon frameworks as superb composite anodes for high-performance sodium-ion batteries, *Small*, 2023, **19**, 2304265.

29 Y. Sun, Z. Lian, Z. Ren, Z. Yao, Y. Yin, P. Huai, F. Zhu, Y. Huang, W. Wen, X. Li, R. Tai and D. Zhu, Proton-dominated reversible aqueous zinc batteries with an ultraflat long discharge plateau, *ACS Nano*, 2021, **15**, 14766–14775.

30 D. Ling, G. Tian, D. Zhang and Q. Wang, Electronic regulation engineering of $(NH_4)_{0.25}WO_3$ anode enables fast and stable rocking-chair zinc-ion batteries, *Nano Lett.*, 2025, **25**, 2684–2692.